Modeling and simulation of viscoelastic film retraction

Modeling and simulation of viscoelastic film retraction

Massimiliano M. Villone*

Dipartimento di Ingegneria Chimica, dei Materiali e della Produzione Industriale, Università di Napoli Federico II, P. le Tecchio 80, 80125 Napoli, Italy

Gaetano D'Avino

Dipartimento di Ingegneria Chimica, dei Materiali e della Produzione Industriale, Università di Napoli Federico II, P. le Tecchio 80, 80125 Napoli, Italy

Ernesto Di Maio

Dipartimento di Ingegneria Chimica, dei Materiali e della Produzione Industriale, Università di Napoli Federico II, P. le Tecchio 80, 80125 Napoli, Italy

Martien A. Hulsen

Department of Mechanical Engineering, Eindhoven University of Technology, Eindhoven 5600 MB, The Netherlands

Pier Luca Maffettone

Dipartimento di Ingegneria Chimica, dei Materiali e della Produzione Industriale, Università di Napoli Federico II, P. le Tecchio 80, 80125 Napoli, Italy

Abstract

In this paper, we investigate the retraction of a circular viscoelastic liquid film with a hole initially present in its center by means of finite element numerical simulations. We study the whole retraction process, aiming at understanding the hole opening dynamics both when the hole does not feel any confinement and when it interacts with the solid wall bounding the film.

*Corresponding author. +39 0817682280

Email address: massimilianomaria.villone@unina.it (Massimiliano M. Villone)

The retraction behavior is also interpreted through a simple toy model, that highlights the physical mechanism underlying the process.

We consider three different viscoelastic constitutive equations, namely, Oldroyd-B, Giesekus (Gsk), and Phan Thien-Tanner (PTT) models, and several system geometries, in terms of the film initial radius and thickness. For each given geometry, we investigate the effects of liquid inertia, elasticity, and flow-dependent viscosity on the dynamics of the hole opening. Depending on the relative strength of such parameters, qualitatively different features can appear in the retracting film shape and dynamics.

When inertia is relevant, as far as the opening hole does not interact with the wall bounding the film, the influence of liquid elasticity is very moderate, and the retraction dynamics tends to the one of Newtonian sheets; when the hole starts to interact with the solid wall, hole radius/opening velocity oscillations are detected. Such oscillations enhance at increasing elasticity. From the morphological point of view, the formation of a rim at the edge of the retracting film is observed. If inertial forces become less relevant with respect to viscous forces, R-oscillations disappear, the hole opening velocity goes through a maximum and then monotonically decays to zero, and no rim forms during the film retraction. Geometrical changes have the effect of enlarging or reducing the portion of the retraction dynamics not influenced by the presence of the solid wall with respect to the one governed by the hole-wall interactions.

Keywords: film retraction, viscoelastic liquid, direct numerical simulations, model

---

1. Introduction

The retraction of liquid sheets is of interest in a wide range of scientific and technological fields, ranging from biological membranes to foam production.[1]

The very first observations of such phenomenon were made on soap bubbles by Dupré [2] and Lord Rayleigh,[3] in the nineteenth century. More than half a century later, an experimental work by Ranz [4] reported that a punctured soap film retracts under the influence of surface tension at an almost constant speed, and, during the retraction, the liquid tends to accumulate in a rim around the opening hole. About ten years later, Taylor [5] and Culick [6] independently derived a mathematical expression for such velocity, which turns out to be $u_{\mathrm{TC}} = \sqrt{2\Gamma/(\rho h)}$, with Γ the surface tension between the liquid and the ambient fluid, ρ the liquid density, and h the film thickness. McEntee and Mysels [7] provided experimental validation of Taylor-Culick theory for soap films thicker than 0.1 μm, while Keller [8] extended the theory to sheets of non-uniform thickness.

At the end of last century, Debrégeas et al. [9, 10] performed experiments on PDMS sheets, and found that, when the liquid is highly viscous, the retraction is much slower than the one of soap films, and does not occur at constant velocity. They also derived an exponential law for the hole radius growth, which reads $r(t) = R_0 \exp[\Gamma t/(\eta h)]$, where R_0 is the initial hole radius (as soon as the film gets punched) and η is the liquid viscosity. Moreover, no rim was observed during the retraction in PDMS films.

Brenner and Gueyffier [11] studied the retraction of a planar liquid sheet by means of the lubrication theory, finding that the rim formation depends

on the relative weight of viscosity, surface tension and inertia, and identified a dimensionless parameter that gives a measure of the interplay of such effects, namely, the Ohnesorge number $\mathrm{Oh} = \eta/\sqrt{2\Gamma\rho h}$. In particular, the rim is observed at low Oh-values, whereas it does not appear at large Oh. Song and Tryggvason [12] performed numerical simulations that extended the work by Brenner and Gueyffier [11] by taking into account the presence of an ambient fluid surrounding the liquid sheet. Their simulations show that, when the viscosity of the ambient fluid is within 10% of the viscosity of the liquid film, the influence of the ambient fluid is negligible. Further numerical investigations were performed by Sunderhauf et al., [13] where the mechanism of rim formation when inertial or viscous effects are dominant was studied.

Recently, Savva and Bush [14] investigated through the lubrication theory the retraction of unbounded liquid sheets with planar and circular shapes, validating the results from Taylor, [5] Culick, [6] and Debrégeas et al., [9, 10] and elucidating the effects of viscosity, geometry and initial conditions.

All the above mentioned papers, both experimental and theoretical, deal with films made of Newtonian liquids. In this paper, we study the retraction of a discoid viscoelastic liquid film with a hole initially present in its center through finite element numerical simulations. The competition between inertial and elastic effects on the phenomenon is studied. Moreover, both constant-viscosity and flow-depending-viscosity constitutive equations are investigated.

Examining the dynamics of viscoelastic liquid sheets would allow to understand the range of process parameters where liquid elasticity 'counts', which is of interest from both a scientific and a technological point of view,

since many industrial problems, e.g., polymer foaming, deal with films involving viscoelastic liquids. We investigate under what process conditions the unbounded retraction velocity, i.e., the hole opening velocity when the hole does not interact yet with the bounding wall, is significantly influenced by the elasticity of the liquid with respect to the Newtonian case. The numerical results are interpreted by means of a simple heuristic model that highlights the physics underlying the retraction process. In addition, we also consider what happens when the opening hole comes in the proximity of the solid wall that bounds the retracting film.

2. Problem outline

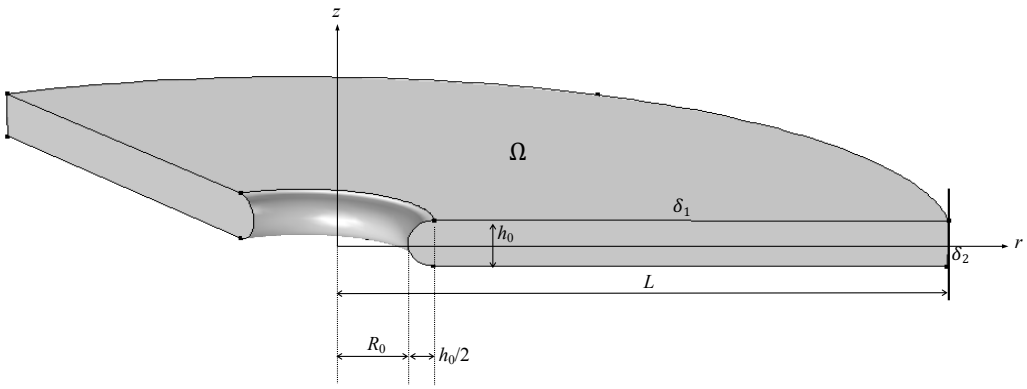

Figure 1: Geometry of a discoid viscoelastic film with radius L and initial thickness h_0. A concentric hole is present with initial radius R_0 and curvature radius $h_0/2$.

Figure 1 sketches the system under investigation: a discoid viscoelastic

liquid film Ω with radius L and initial thickness h_0 has a concentric hole with initial radius R_0. Along the film thickness, the hole has not a uniform radius, as the latter goes from R_0, at the middle of the film, to $R_0 + h_0/2$, at the top and the bottom of the film cross section. The hole has a uniform initial curvature radius $h_0/2$. A cylindrical coordinate system is set with its origin in the center of the hole (and of the film), its r-axis oriented along the film radius, and its z-axis oriented along the film thickness. At $r = L$, the liquid film is in contact with a cylindrical solid wall.

Assuming that the system is isothermal, that the material is incompressible, i.e., the volume of the viscoelastic film is constant, and neglecting the effects of the gravity, the film dynamics is governed by the mass and momentum balance equations in the following form:

$$\boldsymbol{\nabla} \cdot \boldsymbol{u} = 0 \tag{1}$$

and

$$\rho \frac{\partial \boldsymbol{u}}{\partial t} + \rho \boldsymbol{u} \cdot \boldsymbol{\nabla} \boldsymbol{u} = -\boldsymbol{\nabla} p + \eta_{\mathrm{s}} \nabla^2 \boldsymbol{u} + \boldsymbol{\nabla} \cdot \boldsymbol{\tau} \tag{2}$$

where $\boldsymbol{u}$ is the velocity vector, ρ is the density of the liquid, t is the time, p is the pressure, η_{s} is the 'Newtonian' contribution to the liquid viscosity, and $\boldsymbol{\tau}$ is the viscoelastic contribution to the stress tensor, respectively. Notice that, if a Newtonian liquid was considered, the last term in the rhs of Eq. (2) would disappear.

We consider three different viscoelastic constitutive equations, namely, the Oldroyd-B, Giesekus (Gsk) , and exponential Phan Thien-Tanner (PTT) models. [15] The Oldroyd-B model is widely used to describe viscoelastic

liquids with a constant viscosity, and it reads

$$\lambda \overset{\triangledown}{\boldsymbol{\tau}} + \boldsymbol{\tau} = 2\eta_{\mathrm{p}} \boldsymbol{D} \tag{3}$$

with $\overset{\triangledown}{\boldsymbol{\tau}} = \frac{D\boldsymbol{\tau}}{Dt} - (\nabla \boldsymbol{u})^T \cdot \boldsymbol{\tau} - \boldsymbol{\tau} \cdot \nabla \boldsymbol{u}$ the upper-convected time derivative, λ the viscoelastic liquid relaxation time, η_{p} the non-Newtonian contribution to the viscosity of the liquid, and $\boldsymbol{D} = \frac{1}{2}(\nabla \boldsymbol{u} + \nabla \boldsymbol{u}^{\mathrm{T}})$ the symmetric part of the velocity gradient tensor. The Giesekus constitutive equation is commonly employed to describe the rheological behavior of polymer solutions. It can be written as follows:

$$\lambda \overset{\triangledown}{\boldsymbol{\tau}} + \boldsymbol{\tau} + \frac{\lambda \alpha}{\eta_{\mathrm{p}}} \boldsymbol{\tau}^2 = 2\eta_{\mathrm{p}} \boldsymbol{D} \tag{4}$$

where α is the parameter that modulates the dependence of the viscosity on the strain rate. Finally, the exponential Phan Thien-Tanner constitutive equation typically models polymer melts, and reads

$$\lambda \overset{\triangledown}{\boldsymbol{\tau}} + \exp\left[\frac{\lambda \epsilon}{\eta_{\mathrm{p}}} \mathrm{tr}(\boldsymbol{\tau})\right] \boldsymbol{\tau} = 2\eta_{\mathrm{p}} \boldsymbol{D} \tag{5}$$

with ϵ the parameter that modulates the dependence of the viscosity on the strain rate and $\mathrm{tr}(\boldsymbol{\tau})$ the trace of the $\boldsymbol{\tau}$-tensor. Notice that when the parameters α and ϵ go to zero, both the Gsk and the PTT constitutive equations 'degenerate' into the Oldroyd-B model.

The balance equations that describe the system in Fig. 1 are supplied with the following boundary conditions:

$$\boldsymbol{T} \cdot \boldsymbol{n} = \Gamma \, \boldsymbol{n} \boldsymbol{\nabla} \cdot \boldsymbol{n} \quad \text{on } \delta_1 \tag{6}$$

$$\boldsymbol{u} \cdot \boldsymbol{n} = 0 \quad \text{on } \delta_2 \tag{7}$$

$$(\boldsymbol{I} - \boldsymbol{nn}) \cdot (\boldsymbol{T} \cdot \boldsymbol{n}) = \boldsymbol{0} \quad \text{on } \delta_2 \tag{8}$$

In Eq. (6), $\boldsymbol{T} = -p\boldsymbol{I} + 2\eta_s \boldsymbol{D} + \boldsymbol{\tau}$ is the total stress tensor in the fluid, Γ is the surface tension, and $\boldsymbol{n}$ is the outwardly directed unit vector normal to the boundary. Eq. (6) is the condition on stress on the free surfaces of the film, i.e., all the surfaces not in contact with the wall. It is worth remarking that, like in [12], the fluid surrounding the liquid film is not considered in the domain, yet its presence enters the problem through the surface tension Γ in Eq. (6). Equation (7) is the adherence condition between the liquid film and the solid wall at $r = L$ in the r-direction, whereas Equation (8) is the perfect slip condition on the z-component of the velocity at $r = L$. Notice that Eqs. (7)-(8) imply that the length L of the domain shown in Fig. 1 is constant and the film can only slide tangentially to the wall.

We assume that, at $t = 0$, the liquid film is motionless and stress-free, namely,

$$\begin{aligned} \boldsymbol{u}|_{t=0} &= \boldsymbol{0} \quad \text{in } \Omega \\ \boldsymbol{\tau}|_{t=0} &= \boldsymbol{0} \quad \text{in } \Omega \end{aligned} \tag{9}$$

Following Savva and Bush,[14], the model equations are made dimensionless with the film initial thickness h_0 as the characteristic length, $t_i = \sqrt{\rho h_0^3/(2\Gamma)}$ as the characteristic time, the Taylor-Culick velocity $u_{TC} = \sqrt{2\Gamma/(\rho h_0)}$ as the characteristic velocity, and $\hat{\tau} = 2\Gamma/h_0$ as the characteristic stress, with $\eta_0 = \eta_s + \eta_{p0}$ the zero shear total viscosity of the liquid. Notice that t_i is an 'inertial' characteristic time; actually, another characteristic time can be identified, namely, a 'viscous' characteristic time $t_v = \eta_0 h_0/(2\Gamma)$. By means of these two characteristic times, two dimensionless parameters can be defined: the Ohnesorge number $\mathrm{Oh} = \eta_0/(\sqrt{2\rho h_0 \Gamma})$, that expresses the

relative importance of viscous to inertial and surface tension forces (note that the viscosity is the total zero shear viscosity), and the Weissenberg number $\mathrm{Wi} = 2\lambda\Gamma/(\eta_0 h_0)$, that gives the ratio of the fluid relaxation time to the viscous characteristic time t_v. In addition, the viscosity ratio $\beta = \eta_\mathrm{s}/\eta_0$, that measures the relative weight of the Newtonian and non-Newtonian contributions to the viscosity of the liquid can be defined. Therefore, the mass and momentum balance equations, in their dimensionless form, read

$$\boldsymbol{\nabla}^* \cdot \boldsymbol{u}^* = 0 \tag{10}$$

$$\frac{\partial \boldsymbol{u}^*}{\partial t^*} + \boldsymbol{u}^* \cdot \boldsymbol{\nabla}^* \boldsymbol{u}^* = -\mathrm{Oh}\boldsymbol{\nabla}^* p^* + \beta \mathrm{Oh} \nabla^{*2} \boldsymbol{u}^* + \mathrm{Oh}\boldsymbol{\nabla}^* \cdot \boldsymbol{\tau}^* \tag{11}$$

The dimensionless Oldroyd-B constitutive equation reads

$$\mathrm{Wi}\overset{\triangledown}{\boldsymbol{\tau}}^* + \boldsymbol{\tau}^* = 2(1-\beta)\boldsymbol{D}^* \tag{12}$$

The dimensionless Gsk constitutive equation can be written as

$$\mathrm{Wi}\overset{\triangledown}{\boldsymbol{\tau}}^* + \boldsymbol{\tau}^* + \frac{\alpha \mathrm{Wi}}{1-\beta}\boldsymbol{\tau}^{2*} = 2(1-\beta)\boldsymbol{D}^* \tag{13}$$

Finally, the PTT constitutive equation, in its dimensionless form, is

$$\mathrm{Wi}\overset{\triangledown}{\boldsymbol{\tau}}^* + \boldsymbol{\tau}^* + \exp\left[\frac{\epsilon \mathrm{Wi}}{1-\beta}\mathrm{tr}(\boldsymbol{\tau}^*)\right]\boldsymbol{\tau}^* = 2(1-\beta)\boldsymbol{D}^* \tag{14}$$

with the superscript * denoting dimensionless quantities. The dimensionless boundary and initial conditions are

$$2\mathrm{Oh}\boldsymbol{T}^* \cdot \boldsymbol{n} = \boldsymbol{n}\boldsymbol{\nabla}^* \cdot \boldsymbol{n} \quad \text{on } \delta_1 \tag{15}$$

$$\boldsymbol{u}^* \cdot \boldsymbol{n} = 0 \quad \text{on } \delta_2 \tag{16}$$

$$(\boldsymbol{I} - \boldsymbol{n}\boldsymbol{n}) \cdot (\boldsymbol{T}^* \cdot \boldsymbol{n}) = \boldsymbol{0} \quad \text{on } \delta_2 \tag{17}$$

$$\begin{aligned} \boldsymbol{u}^*|_{t^*=0} &= \mathbf{0} \quad \text{in } \Omega \\ \boldsymbol{\tau}^*|_{t^*=0} &= \mathbf{0} \quad \text{in } \Omega \end{aligned} \tag{18}$$

All the quantities appearing in the following are dimensionless. For the sake of simplicity, the superscript * is omitted in the following.

3. Numerical technique

The equations presented in the previous Section are solved through the finite element method with an Arbitrary Lagrangian Eulerian (ALE) formulation. The numerical code makes use of stabilization techniques widely described in the literature, such as SUPG and log-conformation.[16, 17, 18] A detailed description of the numerical treatment of a viscoelastic liquid in the presence of inertia can be found in Trofa et al.,[19] whereas details on the algorithm employed to track the film surface are given in Villone et al..[20]

As it is evident from Fig. 1, the system has a symmetry axis coinciding with the z-axis and a symmetry plane parallel to the r-axis at $z = 0$, thus we can exploit such features to reduce the physical domain to a 2D axisymmetric computational domain, which is discretized by means of an unstructured mesh made of triangular elements. In Fig. 2, a zoom of the meshed computational domain in the proximity of the origin of the reference frame is displayed.

During the simulations, as long as the hole broadens and the liquid film retracts towards the solid wall at $r = L$, the elements of the mesh progressively deform; every time the mesh quality, in terms of the shape of the 'worst' element in the domain, goes below a fixed level, a remeshing is performed and the solution is projected from the old mesh to the new one.[21, 22]

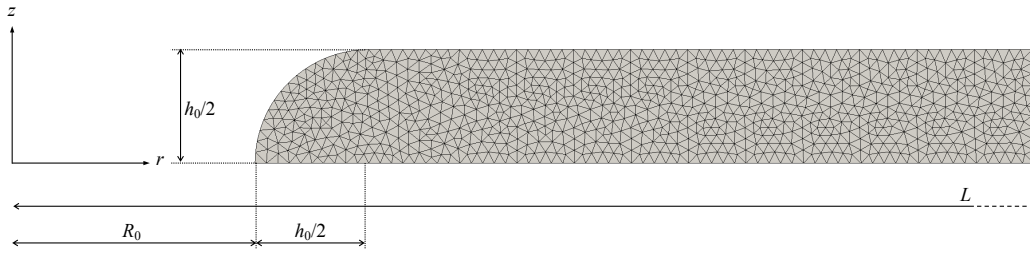

Figure 2: Zoom of the meshed computational domain for the simulation of a circular viscoelastic film with radius L, initial thickness h_0, and initial hole radius R_0.

Before running simulations, convergence tests have been performed in space and time, i.e., mesh resolution and time step for the numerical solution of the equations presented in Section 2 have been chosen such that invariance of the results upon further refinements is ensured. For the simulations presented in this paper, we have found that meshes with a number of triangles from 3×10^4 to 5×10^4 and time steps in the order of $0.01 t_\mathrm{i}$ are adequate. Second order time integration is used.

As a final remark, we report that, due to the mesh resolution required to ensure numerical convergence and to the available computer memory, we cannot simulate films with $L/h_0 >\sim 1000$.

4. Results

A discoid viscoelastic liquid film with radius L and initial thickness h_0 has a concentric hole, whose shape is displayed in Fig. 1, with initial radius R_0 and curvature radius $h_0/2$. Due to the presence of the hole breaking the continuity of the film, the surface tension makes the liquid retract towards the solid wall until reaching the geometrical configuration that minimizes its external surface area. Correspondingly, the hole broadens until reaching its maximum opening, always keeping axial symmetry.

Before considering a viscoelastic film, we report in Fig. 3a, as a validation case, the temporal trends of the hole radius R, normalized by the initial hole radius R_0, for a Newtonian film with $L/h_0 = 950$ and $R_0/h_0 = 50$ at Oh = 10, 50, 100, and we compare them with the lubrication theory predictions from Savva and Bush [14] for unbounded films with the same R_0/h_0- and Oh-values. The solid lines and the circles of the same color correspond to the same Oh. It is apparent that a quantitative agreement is found at short times, which is eventually lost at larger times since in our simulations the liquid film is bounded by a circular solid wall (see Fig. 1 and Eqs. (16)-(17)), whereas Savva and Bush consider a radially infinite film. The lower Oh, the longer the time window where a quantitative agreement holds. At Oh = 10 (the lowest value considered in Fig. 3), the curve and the symbols overlap for the whole time interval considered, then, as Oh increases, such agreement is lost progressively earlier. Of course, in our calculations the hole size reaches a steady value when the retraction is complete.

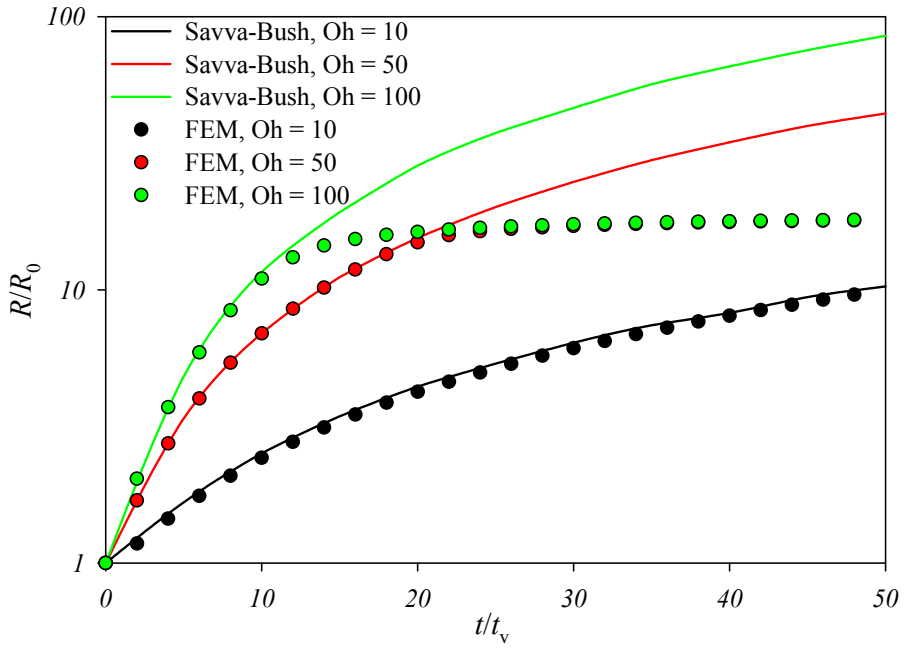

Figure 3: Temporal evolution of the hole radius R, normalized by the initial hole radius R_0, for a Newtonian sheet. Dashed lines: FEM numerical results for a film with $L/h_0 = 950$ and $R_0/h_0 = 50$ at different Oh-values. Solid lines: lubrication theory predictions from Savva and Bush [14] for an unbounded film with the same $R_0/h_0 = 50$ and Oh-values. On the horizontal axis, the time is made dimensionless through the viscous characteristic time $t_v = \eta_0 h_0/2\Gamma$.

4.1. Oldroyd-B liquid

We start our investigation on viscoelastic effects with the constant viscosity Oldroyd-B liquid. All the results reported in this Section, except the ones displayed in Fig. 8, are computed at a value of the viscosity ratio β equal to 0.5.

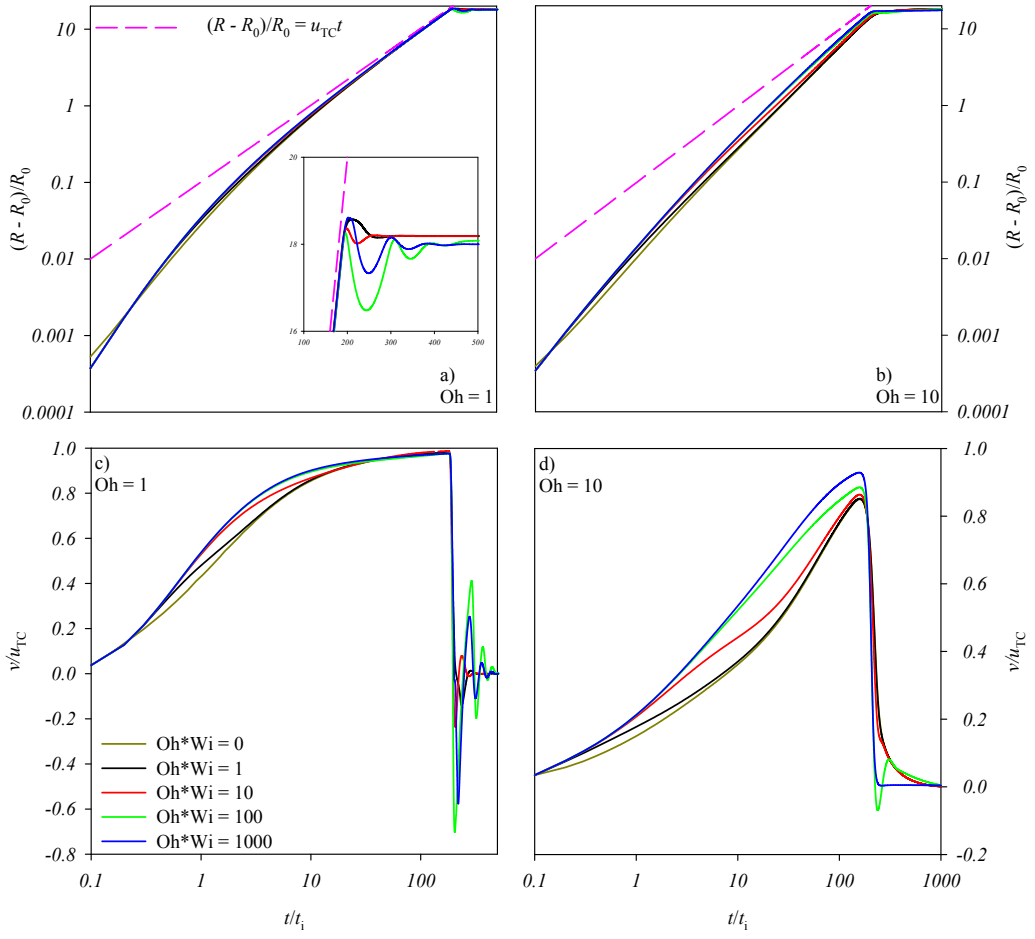

Figure 4: Temporal evolution of the normalized hole radius $(R - R_0)/R_0$ (top row) and of the normalized hole opening velocity v/u_{TC} (bottom row) for a sheet with $L/h_0 = 200$ and $R_0/h_0 = 10$ at Oh = 1 (a - c) and Oh = 10 (b - d). In each panel, results parametric in Oh*Wi are shown. In panels a - b, the pink dashed line shows the prediction from Taylor [5] and Culick. [6] On the horizontal axis, the time is made dimensionless through the inertial characteristic time $t_{\mathrm{i}} = \sqrt{\rho h_0^3/(2\Gamma)}$. Panels a - b: log-log scale; panels c - d: log scale on the t-axis. Inset: linear scale zoom.

4.1.1. Low-Oh

In the top row of Fig. 4, the temporal trends of the normalized hole radius $(R-R_0)/R_0$ are shown for several orders of magnitude of the Ohnesorge times the Weissenberg number at Oh = 1 (panel a) and Oh = 10 (panel b) for a system with $L/h_0 = 200$ and $R_0/h_0 = 10$. In the bottom row, the temporal trends of the hole opening velocity v, namely, the radial velocity computed on the film interface at $z = 0$, normalized by the Taylor-Culick velocity u_{TC}, are displayed for the same values of the parameters as in Figs. 4a-b, respectively. The results for a Newtonian liquid with a viscosity equal to the viscoelastic liquid zero-shear viscosity (Oh*Wi = 0) are also shown in each panel.

The geometrical configuration of the system at complete hole opening is dictated by the minimization of the film external surface area driven by surface tension. The dynamics of the sheet retraction can be conceptually divided in two parts: the short-time/unbounded dynamics, where the hole opening is not influenced by the presence of the solid wall at $r = L$, and the long-time/confined dynamics, which is affected by the interaction between the hole and the wall.

For what matters the short-time dynamics, in Fig. 4a it can be seen that at Oh = 1, almost regardless of the Oh*Wi-value, the hole radius starts below the Taylor-Culick linear prediction (pink dashed line) due to the viscous damping hindering the initial opening, then it tends to 'lean' on such trend until the retracting film feels the solid wall. At this stage, the hole opening trend becomes non-monotonic. More specifically, at Oh*Wi = 0 and Oh*Wi = 1, $(R-R_0)/R_0$ has an overshoot, at Oh*Wi = 10, a couple of small damped oscillations can be detected, and, at Oh*Wi = 100 and Oh*Wi = 1000,

wider damped oscillations are visible (see the linear scale box in Fig. 4a). Therefore, when inertia is relevant (i.e., at low Oh), an increasing elasticity of the liquid makes the film 'bounce' while opening. Of course, the presence of a solid wall at $r = L$ is a necessary condition for the rebounds to appear. By looking at the retraction velocity, it can be observed that the trends at different Oh*Wi-values all tend to unity, which corresponds to the Taylor-Culick velocity that the hole would indefinitely keep if there was no solid wall bounding the film. However, the growth to such level is influenced by Oh*Wi: all the curves start together, then the one that identifies the Newtonian liquid detaches from the viscoelastic ones; subsequently, the curves at non-zero Oh*Wi detach from the others in ascending Oh*Wi order and tend to lie on the Newtonian curve. At t almost equal to L/h_0, for every Oh*Wi, v falls almost instantaneously, becoming negative, then it undergoes damped oscillations around $v = 0$ until R has reached its final value. The amplitude of the v-oscillations depends on Oh*Wi in the same way as the amplitude of the $(R - R_0)/R_0$-oscillations shown above.

At Oh = 10, the evolution of the hole radius (Fig. 4b) has a qualitatively similar dynamics to the case at Oh = 1, yet the curves at different Oh*Wi-values do not have enough time to reach the Taylor-Culick curve before the hole gets close to the wall. On the other hand, v (Fig. 4d) starts less steeply than at Oh = 1 and it does not approach the unit value. The v-trends are influenced by Oh*Wi analogously to the case at Oh = 1: all the curves start together, then they detach from each other in ascending Oh*Wi order, tending to the Newtonian curve; however, unlike in Fig. 4c, only the curves at Oh*Wi = 1, 10 partially overlap the Newtonian one. For every Oh*Wi

considered, the retraction velocity reaches a maximum at $t/t_{\rm i} \simeq L/h_0$, then it decreases until becoming null due to the presence of the solid wall that stops the film retraction. Except the case at Oh*Wi = 100 (green curve), v goes to 0 monotonically. The height of the v-maximum increases with Oh*Wi.

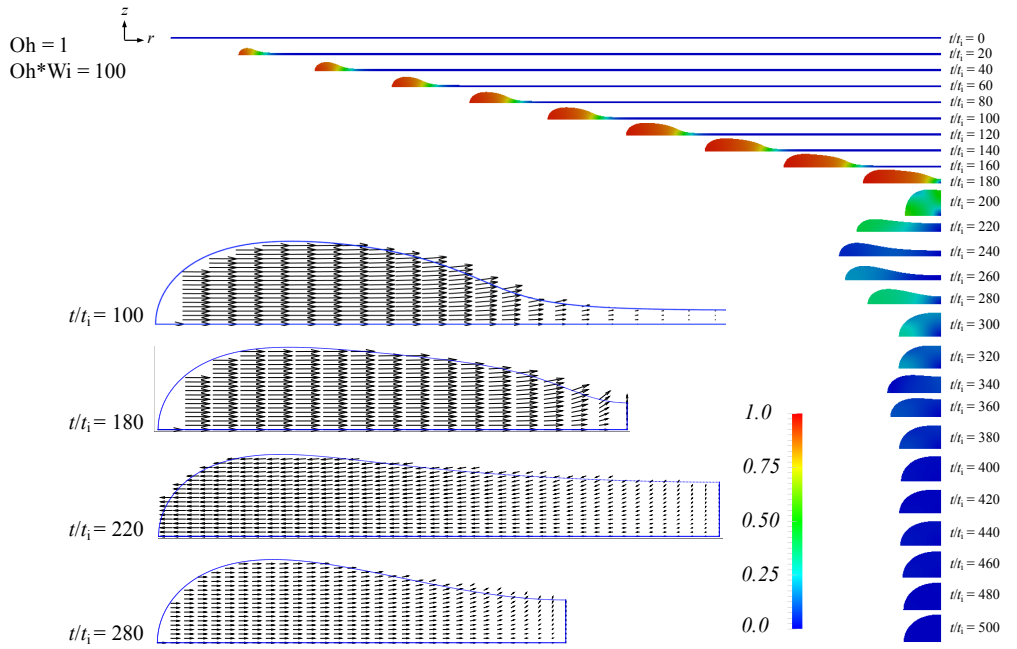

Figure 5: Evolution of the morphology of a film with $L/h_0 = 200$ and $R_0/h_0 = 10$ at Oh = 1 and Oh*Wi = 100. The color scale refers to the magnitude of the normalized liquid velocity $v/u_{\rm TC}$. In the lower left corner, the velocity vector field in the film cross section is shown at four times. The time is made dimensionless through the inertial characteristic time $t_{\rm i} = \sqrt{\rho h_0^3/(2\Gamma)}$.

Let us investigate the morphology of the liquid film during the retraction. In Fig. 5, we show a sequence of snapshots, taken every 20 inertial time units, of the cross section of the retracting film at Oh = 1, Oh*Wi = 100. Under these conditions, a rim forms at the edge of the liquid film,

whose length and height increase until the hole radius reaches a maximum ($t/t_\mathrm{i} = 200$). Savva and Bush [14] found that, when inertia is relevant, a rim forms in Newtonian films too. The color scale referring to the normalized liquid velocity magnitude shows that the velocity in the retracting film is significantly different from zero only in the rim, and keeps almost constant and close to unity, i.e., to u_TC in non-normalized terms, until the maximum opening (see also Fig. 4a). Then, after $t/t_\mathrm{i} = 200$, the damped oscillations of the film are visible. In the lower left corner of Fig. 5, the velocity vector field in the film cross section is shown at four instants. In the first snapshot, referring to $t/t_\mathrm{i} = 100$, it can be seen that the velocity vectors in the rim point right, since the film is retracting; notice also that, on the right of the rim, the vectors also have a positive z-component, because at that time the height of the rim is increasing. The second snapshot is taken at $t/t_\mathrm{i} = 180$, where the hole radius has almost reached its maximum value, and the film is about to bounce back. Then, in the third snapshot, taken at $t/t_\mathrm{i} = 220$, the film has reversed its velocity and is stretching, as the velocity vectors pointing left indicate. During the rebounds, the liquid velocity magnitude decays, as it emerges comparing the length of the arrows between the previous snapshots. Finally, in the fourth snapshot, referring to $t = 280$, the film has again reversed its motion direction (vectors point right), while its velocity magnitude continues to decay. At low Oh-values, from the qualitative point of view, all the morphological evolutions at different Oh - Oh*Wi couples can be assimilated to those shown in Fig. 5

At low Oh, changing the geometrical parameters L/h_0 and R_0/h_0 does not alter the qualitative behavior of the film retraction. Quantitatively, the

time needed to reach the final hole opening is proportional to the film radius, whereas the effect of the R_0/h_0-value is of shifting the retraction dynamics in time.

If the hypothesis of perfect slip in the axial direction between the liquid film and the solid wall expressed by Eq. (8) is substituted by a partial-slip condition, until the hole does not 'feel' the solid wall, there is no difference at all with the total-slip case, then the extent of the slip has a quantitative effect: at decreasing slip, the oscillations of the hole radius are increasingly damped.

4.1.2. High-Oh

In the top row of Fig. 6, the temporal evolution of the normalized hole radius $(R - R_0)/R_0$ is displayed for several orders of magnitude of Oh*Wi at Oh = 100 (panel a) and Oh = 1000 (panel b). In Figs. 6c-d, the temporal trends of the normalized hole opening velocity v/u_{TC} are reported for the same parameter values as in Figs. 4a-b, respectively.

In Fig. 6a, it can be observed that, at short time, all the curves at different Oh*Wi start below the exponential growth prediction from Debrégeas et al. [9, 10] (orange dashed line), then the curves at Oh*Wi = 0 (Newtonian), 1, and 10 tend to overlap the orange line until the normalized hole radius detach from it and tends to the final value at complete hole opening; on the contrary, at Oh*Wi = 100 and 1000, a quantitatively appreciable difference can be seen between the R-trends of the viscoelastic films and the exponential law. For all the Oh*Wi-values considered, the hole radius gets to its final value monotonically and no bounces are detected due to the hole-wall interaction. From the retraction velocity point of view, Fig. 6c shows that,

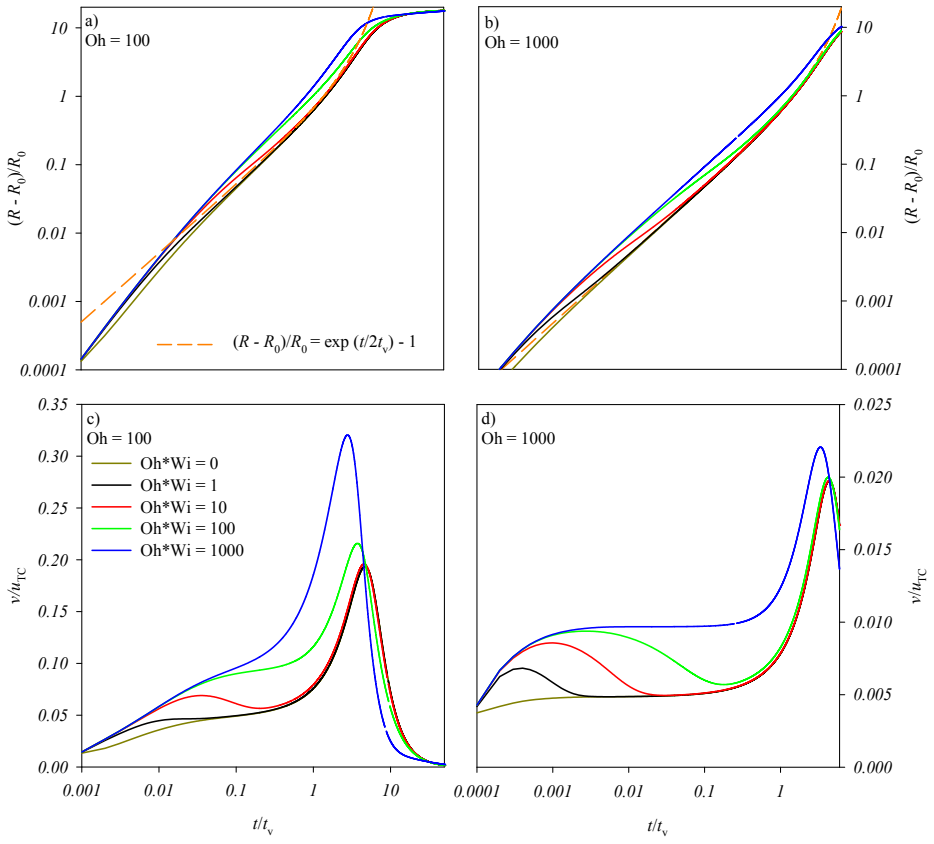

Figure 6: Temporal evolution of the normalized hole radius $(R-R_0)/R_0$ (top row) and of the normalized hole opening velocity v/u_{TC} (bottom row) for a sheet with $L/h_0 = 200$ and $R_0/h_0 = 10$ at Oh = 100 (a - c) and Oh = 1000 (b - d). In each panel, results parametric in Oh*Wi are shown. In panels a - b, the orange dashed line shows the prediction from Debrégeas et al.. [9, 10] On the horizontal axis, the time is made dimensionless through the viscous characteristic time $t_{\mathrm{v}} = \eta_0 h_0/2\Gamma$. Panels a - b: log-log scale; panels c - d: log scale on the t-axis.

for every Oh*Wi, v grows to a maximum, then it decays to 0 because of the wall stopping the hole opening. The Oh*Wi-value has an evident quantitative effect on the position and the height of the maximum: indeed, as

Oh*Wi increases, the maximum occurs earlier and is higher. In addition, a peculiar behavior in the hole opening velocity can be observed at short times depending on Oh*Wi: at Oh*Wi = 1 and 10, v attains a relative maximum, afterwards it decreases and overlaps the Newtonian trend at Oh*Wi = 0; instead, at Oh*Wi = 100, 1000, the growth to the peak is monotonic, yet a concavity-change can be detected, and a significant distance is observed with respect to the Newtonian case.

At Oh = 1000 (Fig. 6b), the $(R - R_0)/R_0$ temporal trends at different Oh*Wi start closer to the exponential curve from Debrégeas et al. than at Oh = 100, and, for Oh*Wi $\leq$ 100, they tend to lie on such curve until wall effects start to play a role in the hole opening; only at Oh*Wi = 1000 a quantitatively appreciable difference can be seen between the hole radius trend of the viscoelastic sheet and the orange dashed line. As at Oh = 100, no bounces are detected during the hole opening. The retraction velocity curves at Oh = 1000 are shown in Fig. 6d. As at Oh = 100, the v-trends show a maximum before decaying to 0. The short time-dynamics is very interesting, as the Newtonian case (Oh*Wi = 0) and the 'most elastic' case (Oh*Wi = 1000) both have a velocity plateau, yet at different levels; the other curves at nonzero Oh*Wi all start as the one at Oh*Wi = 1000, then they detach from the latter in increasing Oh*Wi order and, going through a relative maximum, they overlap the Newtonian trend.

In Fig. 7, the cross section of the retracting film is visualized through a sequence of snapshots taken every 50 viscous time units at Oh = 100 and Oh*Wi = 100. At variance with what shown in Fig. 5, here no rim forms at the edge of the liquid film during the retraction. In other words,

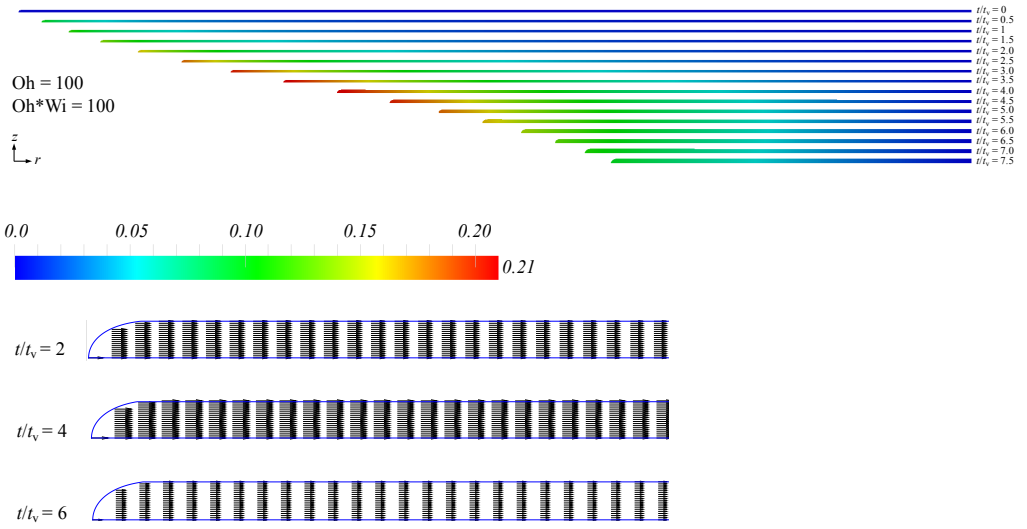

Figure 7: Evolution of the morphology of a film with $L/h_0 = 200$ and $R_0/h_0 = 10$ at Oh = 100 and Oh*Wi = 100. The color scale refers to the magnitude of the normalized liquid velocity v/u_{TC}. At the bottom, the velocity vector field in the film cross section is shown at three times. The time is made dimensionless through the viscous characteristic time $t_{\mathrm{v}} = \eta_0 h_0/2\Gamma$

as the hole radius increases, the height of the film increases uniformly along the r-direction. Moreover, the hole radius monotonically increases, and no oscillations are observed. From the color scale showing the magnitude of the liquid velocity, it is visible how the velocity first grows, reaches a maximum at around 4 viscous time units, and finally decays to 0 as the hole is approaching the final opening (as also reported in Fig. 6c). At the bottom of Fig. 7, the velocity vector field in the film cross section is shown at three times ($t/t_{\mathrm{v}} = 2, 4, 6$). In all the three snapshots, the velocity vectors in the film point right since the hole radius monotonically increases. In the second snapshot, taken at $t/t_{\mathrm{v}} = 4$, i.e., close to the time when the velocity attains

its maximum value, the arrows are longer than in the first and the third one.

Like at low Oh, quantitative variations in the geometrical parameters L/h_0 and R_0/h_0 do not have qualitative effects on the sheet retraction dynamics. Given R_0/h_0, increasing L/h_0 postpones the hole interaction with the bounding wall and the occurrence of the v-maximum, thus increasing the peak height, since the opening film feels the wall 'later'.

At high Oh, the replacement of the perfect slip condition given by Eq. (8) by a partial-slip condition has no relevant qualitative nor quantitative effects.

Finally, the effect of the viscosity ratio is investigated. In Fig. 8, the normalized retraction velocity v/u_{TC} is displayed as a function of the time divided by the viscous time for a film with $L/h_0 = 200$, $R_0/h_0 = 10$, and Oh = 1000. In the above mentioned figure, 5 Oh*Wi-values are considered, i.e., Oh*Wi = 0, 1, 10, 100, 1000, and, for the viscoelastic liquid, 3 values of the viscosity ratio: $\beta = 1/3, 0.5, 2/3$. We point out that the solid lines with circles in Fig. 8 are the same as in Fig. 6d. From the qualitative point of view, changing β does not alter the shape of the velocity trends corresponding to the different Oh*Wi considered, yet some quantitative effects are clearly visible: for Oh*Wi = 1, 10, 100, increasing β, thus increasing the weight of the 'Newtonian' viscosity η_{s} with respect to the 'non-Newtonian' viscosity η_p, given the zero-shear viscosity η_0, lowers the height of the relative v-maximum occurring at short time, and makes the v-trend collapse earlier on the Newtonian trend and the exponential prediction (until wall effects start to play a role); at Oh*Wi = 1000, increasing β lowers the plateau velocity attained by the opening hole before the rise to the absolute peak, making the

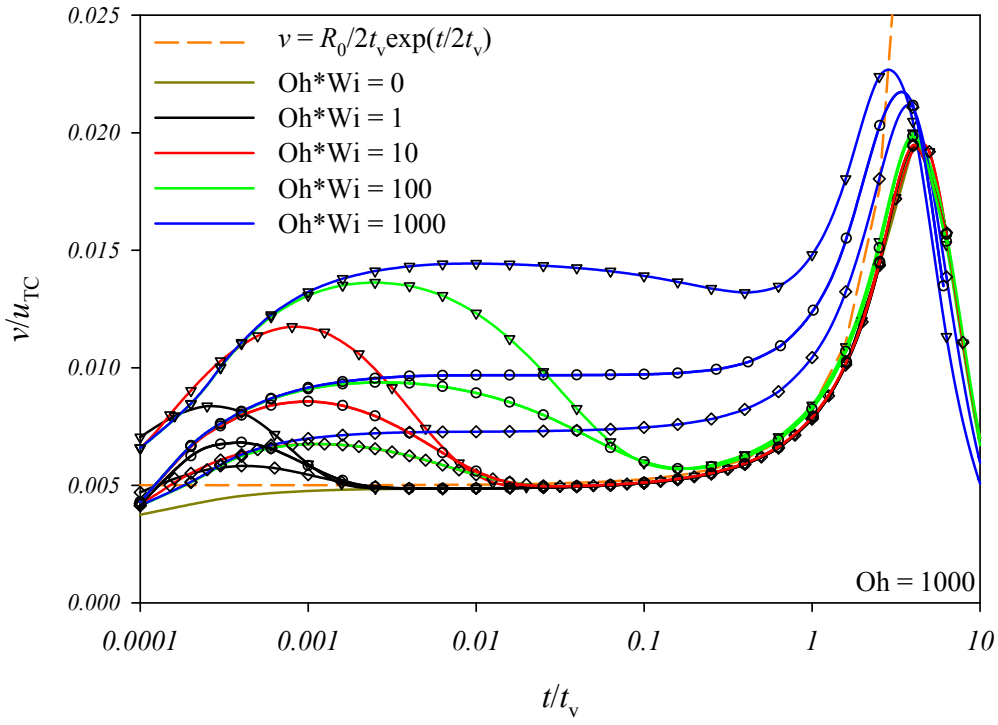

Figure 8: Temporal evolution of the normalized hole opening velocity v/u_{TC} for a sheet with $L/h_0 = 200$ and $R_0/h_0 = 10$ at Oh = 1000. 5 Oh*Wi-values (Oh*Wi = 0, 1, 10, 100, 1000, see the color legend) and 3 values of the viscosity ratio ($\beta = 1/3$ (triangles), 0.5 (circles), 2/3 (diamonds)) are shown. The orange dashed line shows the prediction from Debrégeas et al.. [9, 10] On the horizontal axis, the time is made dimensionless through the viscous characteristic time $t_{\mathrm{v}} = \eta_0 h_0/2\Gamma$. Log scale on the t-axis.

velocity trend of the viscoelastic liquid progressively closer to the Newtonian one.

4.1.3. Toy model

A very simple heuristic one-dimensional model, inspired by that proposed by Debrégeas et al., [10] might be used to rationalize some simulation findings. The circular film has a hole of radius R_0 at its center at the initial condition. The liquid is treated as incompressible, and we neglect inertia, thus the initial dynamics at short times will be excluded. The film is initially at rest and stress-free, and retracts from the round tip for capillary force (to leading order, 2Γ per unit azimuthal length), which is resisted by the radial viscoelastic stress in the sheet. The flow is essentially extensional. In the limit of large Oh, the film retracts without the formation of rims, so the film thickness is treated as uniform. The liquid behaves as an Oldroyd-B liquid, with a Maxwell unit (a dashpot with a characteristic viscosity η_{p0} in series with a spring with modulus $G = \eta_{\mathrm{p0}}/\lambda$) in parallel with another dashpot (with a characteristic viscosity η_{s}). Of course, $\eta_{\mathrm{s}} + \eta_{\mathrm{p0}}$ again is the total zero shear viscosity η_0 (see Sec. 2). Let $R(t)$ represent the current hole radius. The liquid retracts at a speed $\dot{R}(t) = v(t)$. The dimensionless scales are h_0 (the initial film thickness) for length, $t_{\mathrm{v}} = \eta_0 h_0/(2\Gamma)$ for time, $2\Gamma h_0$ for forces. In nondimensional form, the model is written as

$$\mathrm{Wi}\dot{R}_{\mathrm{MD}} = R - R_{\mathrm{MD}} \tag{19}$$

$$2h(1-\beta)\dot{R}_{\mathrm{MD}} + 2h\beta\dot{R} = R \tag{20}$$

with the initial conditions $R(0) = R_{\mathrm{MD}}(0) = R_0$.

In Eqs. (19) - (20), R_{MD} is the dimensionless current position of the Maxwell dashpot and h is the dimensionless actual thickness of the film. The parameters appearing in Eqs. (19) - (20) are the Weissenberg number

Wi and the viscosity ratio β. It is worth remarking that, in the Oh $\gg 1$ limit, the Ohnesorge number does not appear in the problem, as already noted by Savva and Bush. [14] In order to account for bounded geometries, the current film thickness h can be computed, as suggested by Debrégeas et al., [9, 10] by applying a simple mass balance, so that the moving volume of liquid resulting from the hole growth is uniformly distributed over the entire film. In dimensionless terms, the current film thickness, then, is

$$h = \frac{L^2 - R_0^2}{L^2 - R(t)^2} \tag{21}$$

where L is the position of the solid wall encircling the liquid. The unbounded situation is recovered in the limit of $L \to \infty$, and gives $h = 1$.

For unbounded films, the model can be solved analytically. In such a case, its Newtonian version (which is easily obtained by removing the Maxwell arm) gives the well known exponential growth of the hole radius $R_0 \exp[\Gamma t/(\eta_s h_0)]$ (that, in our dimensionless terms, reads $R_0 \exp[t/2]$). The dimensionless Newtonian velocity is, of course, $R_0/2 \exp[t/2]$. Instead, for what matters a viscoelastic liquid, the model prediction for the velocity is

$$v = R_0 e^{\frac{t(\mathrm{Wi}-2)}{4\beta \mathrm{Wi}}} \frac{\left[(4\beta + \mathrm{Wi} - 2)\sinh\left(\frac{Kt}{4\beta \mathrm{Wi}}\right) + K\cosh\left(\frac{Kt}{4\beta \mathrm{Wi}}\right)\right]}{2\beta K} \tag{22}$$

with $K = \sqrt{\mathrm{Wi}(8\beta + \mathrm{Wi} - 4) + 4}$. Of course, at Wi $= 0$ and $\beta = 1$, the Newtonian velocity is correctly recovered.

Figure 9a shows the hole opening velocity, normalized by the Taylor-Culick velocity u_{TC}, versus dimensionless time in the unbounded case at Oh $= 1000$, $\beta = 0.5$, and different Wi−values. The initial trend of all the

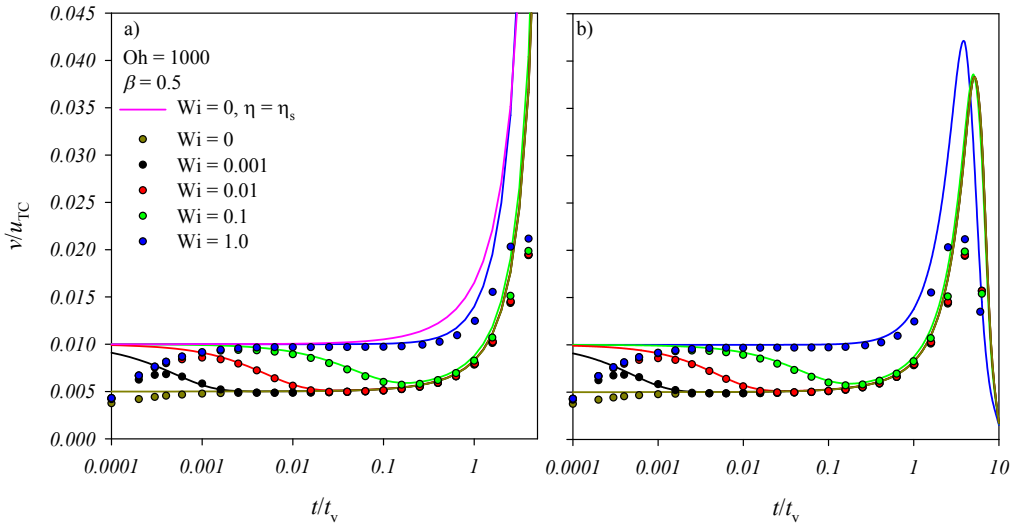

Figure 9: Temporal evolution of the normalized hole opening velocity v/u_{TC} for a sheet with $R_0/h_0 = 10$ at Oh = 1000, $\beta = 0.5$, and Wi = 0, 0.001, 0.01, 0.1, 1.0. Solid lines: heuristic model predictions for an unbounded film(a) and for a film with $L/h_0 = 200$ (b); symbols: finite element numerical results for a film with $L/h_0 = 200$. On the horizontal axis, the time is made dimensionless through the viscous characteristic time $t_{\mathrm{v}} = \eta_0 h_0/2\Gamma$. Log scale on the t-axis.

curves at nonzero Wi coincides with the Newtonian behavior with a viscosity equal to η_{s}, then two different dynamics are observed: for Wi < 1, the curves get close to the Newtonian one with viscosity η_0; for Wi > 1, the curves remain close to the corresponding Newtonian case with viscosity η_{s}, but following a slightly slower pace. The hole growth speed, correspondingly, starts from the same jump at $t = 0^+$ (we recall that there is no inertia in the model) and then follows two different dynamics: for Wi < 1, the speed initially decreases, reaches a minimum, and then starts growing (the lower the Wi - value, the closer the final behavior to that of the Newtonian film with

$\eta = \eta_s$); on the contrary, for $\mathrm{Wi} = 1$ no minimum is observed. Equation (22) yields that the limiting value of the hole growth speed at $t = 0$ is $R_0/(2\beta)$, while the velocity slope is $R_0(2\beta + \mathrm{Wi} - 2)/(4\beta^2\mathrm{Wi})$. Hence, it is apparent that $\mathrm{Wi} = 2(1-\beta)$ (which is equal to 1 when β is equal to 0.5) marks a critical condition: a negative slope is obtained for $\mathrm{Wi} < 2(1-\beta)$, whereas a positive one is obtained for $\mathrm{Wi} > 2(1-\beta)$. The behavior predicted by the toy model is in good agreement with the initial behavior obtained through simulations (see the circles in Fig. 9a that reproduce the results shown in Fig. 6d). Of course, since the simulation results contain inertial effects too, the retraction velocity always starts from zero, but, starting from the relative maximum, the finite element numerical findings are in quantitative agreement with the trends predicted by the toy model. Also the numerical trends pass through a minimum only for $\mathrm{Wi} < 2(1-\beta) = 1$. It should be remarked that this latter behavior, arising from both the heuristic model and the simulation results, gives a possible explanation to the experimental evidences reported by Roth et al., [23] who observed that the retraction is faster at its onset, then it slows down. Our results would support the conclusion that what they observed is coherent with the dynamics at $\mathrm{Wi} < 2(1-\beta)$.

Believing in the capabilities of our simple model, the agreement observed at high Oh between model and simulation results until $t \sim 1$ implies that the dynamics up to that time value is unaffected by the film thickness, thus it could be considered 'unbounded'. On the other hand, if a film extending up to $R = L$ is considered and the film thickness variation is introduced in the model, one might extend the model predictive capabilities even to bounded conditions. Figure 9b reports the model predictions in the same conditions

as in Fig. 9a for $L = 200$ and accounting for thickness dynamics. It is evident that a qualitative agreement with the simulation results is found. Indeed, the retraction velocity passes through a maximum and then decays to zero. The position in time of the maximum is correctly predicted. In view of the simplicity of the model, we can say that the stopping of hole growth is due, in this case, to a viscous brake: as the thickness increases, the interfacial 'driving' term becomes, progressively, less and less effective. A simple correction to the viscous terms in Eqs. (19) - (20) with a factor $f(h)$ makes the toy model predictions almost overlap the simulation results (not shown here); this correction is justified as to account for the weight of hoop stresses when the hole enlarges.

As mentioned above, in the high Oh limit, the Ohnesorge number does not appear in the problem, its effect being just a scale. This means that the same model predictions can be remapped on top of the simulation results at different Oh-values.

Finally, the effect of the viscosity ratio β on the toy model predictions is reported in Fig. 10, where the velocity curves are shown at $Oh = 1000$, $Wi = 1$, and $\beta = 1/3, 0.5, 2/3$. It is apparent that, given the other parameters, the hole growth speed at $t = 0$ decreases at increasing β, (we recall that Eq. (22) predicts $v(t = 0) = R_0/(2\beta)$). In addition, it can be pointed out that, since for $\beta = 1/3$ the condition Wi $< 2(1 - \beta)$ is satisfied, a retraction velocity minimum is detected in the black curve, whereas no minima are present in the curves at $\beta = 0.5, 2/3$, for which Wi $\geq 2(1-\beta)$. A qualitative agreement with the finite element results still holds.

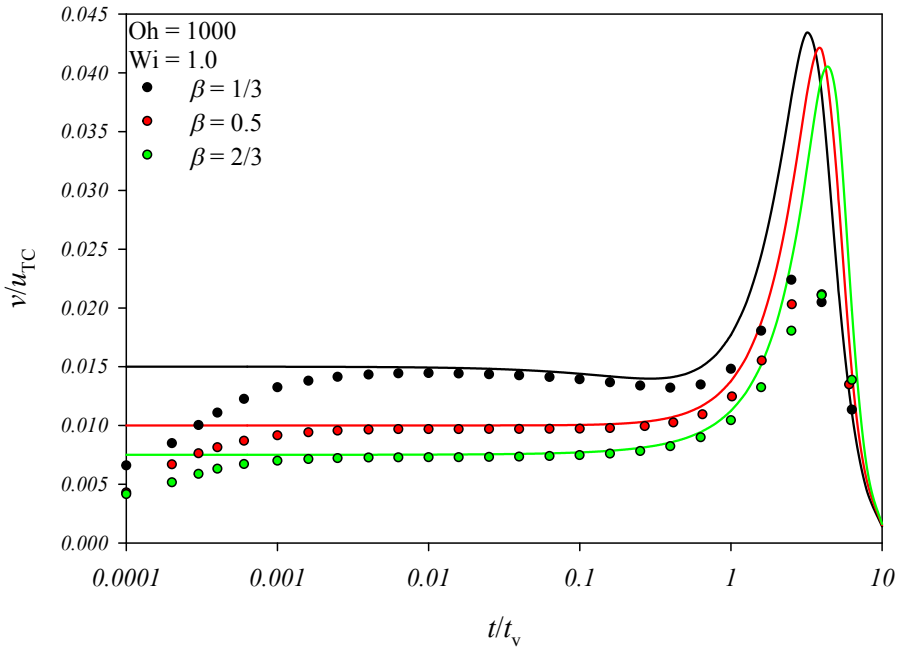

Figure 10: Temporal evolution of the normalized hole opening velocity v/u_{TC} for a sheet with $L/h_0 = 200$, $R_0/h_0 = 10$ at Oh $= 1000$, Wi $= 1.0$, and $\beta = 1/3, 0.5, 2/3$. Solid lines: heuristic model predictions; symbols: finite element numerical results. On the horizontal axis, the time is made dimensionless through the viscous characteristic time $t_{\mathrm{v}} = \eta_0 h_0/2\Gamma$. Log scale on the t-axis.

4.2. Giesekus and Phan Thien-Tanner liquids

When films with non-constant-viscosity Gsk and PTT constitutive behaviors are considered, the hole radius dynamics is qualitatively and quantitatively very similar to the one presented above for an Oldroyd-B liquid.

When inertia is relevant, namely, at low Oh, in Gsk and PTT films the hole radius almost stops at a value greater then the final one for a certain time during the retraction, then it goes back and tends to the equilibrium

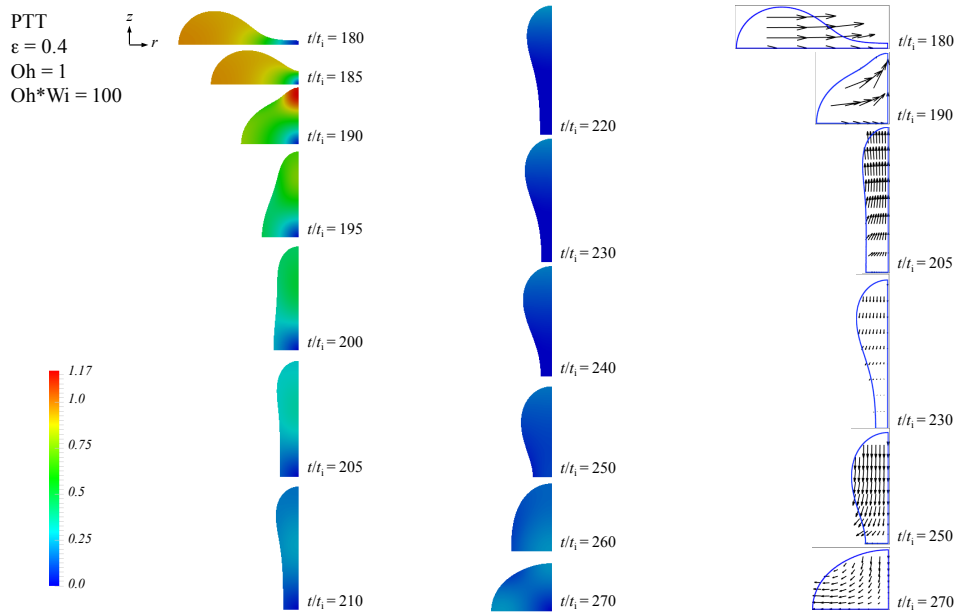

Figure 11: Evolution of the morphology of a Phan Thien-Tanner liquid film with $\epsilon = 0.4$, $L/h_0 = 200$ and $R_0/h_0 = 10$ at Oh $= 1$, Wi $= 100$, $\beta = 0.5$. The color scale refers to the normalized liquid velocity magnitude v/u_{TC}. On the right, the velocity vector field in the film cross section is shown at six times. The time is made dimensionless through the inertial characteristic time $t_{\mathrm{i}} = \sqrt{\rho h_0^3/(2\Gamma)}$.

value dictated by surface tension. The extent of such stop is greater in PTT films than in Gsk films, and in both liquids it increases with the ϵ- and the α-parameter, respectively. This is linked to the film morphology evolution. Figure 11 shows a sequence of snapshots, taken at 13 times between $t/t_{\mathrm{i}} = 180$ and $t/t_{\mathrm{i}} = 270$, of the cross section of the retracting PTT film with $\epsilon = 0.4$. Since in the Gsk liquid and in the PTT liquid with lower ϵ a qualitatively similar scenario occurs, for the sake of brevity, no snapshots of the morphology found in such cases are reported. As the hole radius grows, a rim forms at the edge of the film, whose length and height progressively increase. Unlike the

Oldroyd-B liquid (shown in Fig. 5), a concavity change appears at the extremity of the film profile in the axial direction (see $t/t_\mathrm{i} = 190$). In addition, it can be noticed that, in the proximity of the concavity change, the retraction velocity locally overcomes the Taylor-Culick limit (see the maximum in the v/u_TC color scale). The above mentioned profile concavity change progressively enhances and displaces towards the film symmetry plane at $z = 0$ until the thickness of the film at that coordinate becomes minimum, with the material accumulating far from $z = 0$, thus forming an 'orthogonal rim' (see $t/t_\mathrm{i} = 205 - 220$). At this stage, the film dynamics almost stops, as visible by looking at the film shapes and at the colors representing the velocity magnitude in the film cross section at $t/t_\mathrm{i} = 220, 230$, then the liquid 'comes back' along the z-direction towards $z = 0$, the curvature change in the film profile disappears, and the film evolves towards its final shape (see $t/t_\mathrm{i} = 240 - 270$). The film morphology evolution discussed here explains the above reported statement that the hole radius stays nearly constant for a certain interval of time: indeed, meanwhile the orthogonal rim forms, evolves and disappears, the hole radius stays almost constant. On the right of Fig. 11, the velocity vector field in the film cross section is shown at six time instants. In the first snapshot, taken at $t/t_\mathrm{i} = 180$, it can be seen that, as the film is retracting, the velocity vectors in the rim point right. At $t/t_\mathrm{i} = 190$, the vectors also have a positive z-component, because the film is increasing its dimension in the axial direction. The third snapshot refers to $t/t_\mathrm{i} = 205$, where the velocity vectors are almost vertical and upwardly directed, meaning that the liquid is stretching along the axial direction, and, consequently, squeezing in the radial one. At $t/t_\mathrm{i} = 230$, the length of the arrows is very small, indicating

that the film is almost still, then, at $t/t_\mathrm{i} = 250$, the vectors point down, as the liquid is going towards the symmetry plane at $z = 0$. Finally, in the sixth snapshot, referring to $t/t_\mathrm{i} = 270$, vectors point down and left, since the film is bouncing back towards its equilibrium shape.

5. Conclusions

In this paper, we study through finite element numerical simulations the retraction of a discoid viscoelastic liquid film with a hole initially present in its center. The competitive effects of inertia and elasticity on the phenomenon are investigated systematically. The analysis is carried out for both constant-viscosity (Oldroyd-B) and non-constant-viscosity (Giesekus, Phan Thien-Tanner) viscoelastic liquids, elucidating the effects that a flow-depending viscosity can have on the film retraction. For the Oldroyd-B liquid, when viscous forces overcome inertial ones, the retraction behavior is also interpreted through a simple heuristic model, that highlights the physical mechanism underlying the retraction process.

In an Oldroyd-B liquid, at fixed film radius L, film initial thickness h_0, and initial hole radius R_0, the dynamics of the hole opening is governed by the competition among inertial, viscous, and elastic effects, measured by the Ohnesorge (Oh) and Weissenberg (Wi) numbers. When inertia is relevant, i.e., at low Oh, we find that, as far as the opening hole does not interact with the wall bounding the film, the influence of liquid elasticity is very moderate, and the retraction dynamics tends to the one predicted by Taylor [5] and Culick [6] for Newtonian sheets; when the hole starts to interact with the solid wall, the temporal trends of the hole radius become non-

monotonic, with the appearance of damped R-oscillations. In other words, the liquid film 'bounces' while it is opening. Such oscillations are enhanced at increasing elasticity (high Oh*Wi-values). This feature reflects in the retraction velocity trends: at low Oh, the hole opening velocity v first tends to an asymptotic value, then it goes through damped oscillations, during which it also becomes negative, since the hole is temporarily closing. As for R, increasing Oh*Wi promotes wider v-oscillations. In addition, from the morphological point of view, the formation of a rim at the edge of the retracting film can be observed. If inertial forces become less relevant with respect to viscous forces, namely, Oh increases, at low Oh*Wi-values, the unbounded hole opening trends tend to the one predicted by Debrégeas et al. [9, 10] for Newtonian films, but deviations from such prediction appear at increasing Oh*Wi; for what matters the confined dynamics, R-oscillations disappear, and the hole opening velocity goes through a maximum and then monotonically decays to zero. Increasing Oh*Wi-values enhance the peak height. Moreover, no rim forms during the film retraction, so the thickness of the opening sheet keeps uniform along the radial direction. Geometrical changes, in terms of the ratios of the film radius to its initial thickness L/h_0 and of the initial hole radius to the film initial thickness R_0/h_0 have the effect of enhancing or reducing the portion of the retraction dynamics not influenced by the presence of the solid wall with respect to the one governed by the hole-wall interactions.

A simple one-dimensional toy model is used to rationalize simulation findings through the balance of capillary and viscoelastic forces. At high Oh, in its 'unbounded' formulation, the model shows to be able to predict quanti-

tatively the finite element results at varying Wi until the hole is far from the solid wall. Moreover, if a correction accounting for finite film radius is introduced, also the dynamics of the retraction velocity rise to maximum and decay to zero are caught.

In non-constant-viscosity Giesekus (Gsk) and Phan Thien-Tanner (PTT) liquids, when inertia is low (high Oh), no significative differences are detected in the retraction dynamics with respect to the Oldroyd-B liquid, whereas, when inertia is relevant (low Oh), major differences in the film morphology arise in the film-wall interaction with respect to the Oldroyd-B case.

Acknowledgements

Elasticity in Bubble Breaking (ELTYBUNG) Project funded by the University of Naples Federico II is acknowledged for partial support of this work.

References

[1] P. G. de Gennes, F. Brochard-Wyart, D. Quere, Capillarity and wetting phenomenon, Springer, New York, 2003.

[2] M. A. Dupré, Sixième memoire sur la theorie méchanique de la chaleur, Ann. Chim. Phys. 4 (11) (1867) 194–220.

[3] L. Rayleigh, Some applications of photography, Nature 44 (1133) (1891) 249–254.

[4] W. Ranz, Some experiments on the dynamics of liquid films, J. Applied Phys. 30 (12) (1959) 1950–1955.

[5] G. Taylor, The dynamics of thin sheets of fluid. iii. disintegration of fluid sheets, Proc. R. Soc. Lond. A 253 (1274) (1959) 313–321.

[6] F. Culick, Comments on a ruptured soap film, J. Applied Phys. 31 (6) (1960) 1128–1129.

[7] W. R. McEntee, K. J. Mysels, Bursting of soap films. i. an experimental study, J. Phys. Chem. 73 (9) (1969) 3018–3028.

[8] J. B. Keller, Breaking of liquid films and threads, Phys. Fluids 26 (12) (1983) 3451–3453.

[9] G. Debrégeas, P. Martin, F. Brochard-Wyart, Viscous bursting of suspended films, Phys. Rev. Lett. 75 (21) (1995) 3886.

[10] G. Debrégeas, P. G. De Gennes, F. Brochard-Wyart, The life and death of" bare" viscous bubbles, Science 279 (5357) (1998) 1704–1707.

[11] M. P. Brenner, D. Gueyffier, On the bursting of viscous films, Phys. Fluids 11 (1999) 737–739.

[12] M. Song, G. Tryggvason, The formation of thick borders on an initially stationary fluid sheet, Phys. Fluids 11 (9) (1999) 2487–2493.

[13] G. Sünderhauf, H. Raszillier, F. Durst, The retraction of the edge of a planar liquid sheet, Phys. Fluids 14 (1) (2002) 198–208.

[14] N. Savva, J. W. Bush, Viscous sheet retraction, J. Fluid Mech. 626 (2009) 211–240.

[15] R. G. Larson, Constitutive Equations for Polymer Melts and Solutions: Butterworths Series in Chemical Engineering, Butterworth-Heinemann, 1988.

[16] R. Guénette, M. Fortin, A new mixed finite element method for computing viscoelastic flows, J. Non-Newtonian Fluid Mech. 60 (1) (1995) 27–52.

[17] A. C. Bogaerds, A. M. Grillet, G. W. Peters, F. P. Baaijens, Stability analysis of polymer shear flows using the extended pom–pom constitutive equations, J. Non-Newtonian Fluid Mech. 108 (1) (2002) 187–208.

[18] A. N. Brooks, T. J. Hughes, Streamline upwind/petrov-galerkin formulations for convection dominated flows with particular emphasis on the incompressible navier-stokes equations, Comp. Meth. Appl. Mech. Eng. 32 (1) (1982) 199–259.

[19] M. Trofa, M. Vocciante, G. D'Avino, M. A. Hulsen, F. Greco, P. L. Maffettone, Numerical simulations of the competition between the effects of inertia and viscoelasticity on particle migration in poiseuille flow, Comput. Fluids 107 (2015) 214–223.

[20] M. M. Villone, M. A. Hulsen, P. D. Anderson, P. L. Maffettone, Simulations of deformable systems in fluids under shear flow using an arbitrary lagrangian eulerian technique, Comput. Fluids 90 (2014) 88–100.

[21] H. H. Hu, N. A. Patankar, M. Y. Zhu, Direct numerical simulations of fluid–solid systems using the arbitrary lagrangian–eulerian technique, J. Comput. Phys. 169 (2) (2001) 427–462.

[22] N. O. Jaensson, M. A. Hulsen, P. D. Anderson, Stokes–cahn–hilliard formulations and simulations of two-phase flows with suspended rigid particles, Comput. Fluids 111 (2015) 1–17.

[23] C. Roth, B. Deh, B. Nickel, J. Dutcher, Evidence of convective constraint release during hole growth in freely standing polystyrene films at low temperatures, Phys. Rev. E 72 (2) (2005) 021802.